Ultra-Low Noise Measurements of Ionic Transport Within Individual Single-Walled Carbon Nanotubes

Laure Bsawmaii, Clément Delacou, Valerii Kotok, Sébastien Méance, Koutayba Saada, M Amine Kribeche, Saïd Tahir, Christophe Roblin, Manoel Manghi, John Palmeri, et al.

Journal Name

Ultra-Low Noise Measurements of Ionic Transport Within Individual Single-Walled Carbon Nanotubes[†]

Laure Bsawmaii,[a] Clément Delacou,[a] Valerii Kotok,[a,b] Sébastien Méance,[a] Koutayba Saada,[a] M. Amine Kribeche,[a] Saïd Tahir,[a] Christophe Roblin,[a] Manoel Manghi,[c] John Palmeri,[a] François Henn,[a] Adrien Noury,[a] and Vincent Jourdain[a]

Despite 15 years of extensive investigation, the fabrication and study of nanofluidic devices that incorporate a single carbon nanotube (CNT) still represents a remarkable experimental challenge. In this study, we present the fabrication of nanofluidic devices that integrate an individual single-walled CNT (SWCNT), showcasing a notable reduction in noise by $1-3$ orders of magnitude compared to conventional devices. This achievement was made possible by employing high dielectric constant materials for both the substrate and the CNT-covering layer. Furthermore, we provide a detailed account of the crucial factors contributing to the successful fabrication of SWCNT-based nanofluidic devices that are reliably leak-free, plug-free, and long-lived. Key considerations include the quality of the substrate-layer interface, the nanotube opening, and the effective removal of photoresist residues and trapped microbubbles. We demonstrate that these devices, characterized by a high signal-to-noise ratio, enable spectral noise analysis of ionic transport through an individual SWCNT, thus showing that SWCNTs obey Hooge's law in $1/f$ at low frequencies. Beyond advancing our fundamental understanding of ion transport in SWCNTs, these ultralow-noise measurements open avenues for leveraging SWCNTs in nanopore sensing applications for single-molecule detection, offering high sensitivity and identification capabilities.

Introduction

Due to their unique features, carbon nanotubes (CNTs), and most notably single-walled CNTs (SWCNTs), have attracted significant attention as novel nanofluidic channels. SWCNTs are cylindrical nanostructures with a smooth atom-thin wall only made of sp^2 carbon atoms. Their diameters are typically in the range of $0.8-2$ nm and their length can be adjusted between typically 10 nm and 1 mm. In contrast with other types of nanoholes and nanochannels, SWCNTs are true nano-objects with specific electronic properties which may be used to control or monitor nanofluidic transport. SWCNTs also benefit from a mature technology for the fabrication of highly scaled and complex microdevices. For example, dense parallel arrays of SWCNTs can be grown on a substrate, transferred to another substrate, patterned, electrically connected, and covered using standard microfabrica-

tion tools[1].

Motivated by these unique features, many experimental studies have explored the ionic transport properties of CNTs, notably at the individual nanotube level (see Ref.[2] for a recent review). Lindsay et al.[3]) were the first to report ionic current measurements through individual SWCNTs which showed that the ionic conductance was $2-3$ orders of magnitude larger than the bulk conductance of the electrolyte. Since then, the reported experimental and simulation data support that this giant ionic conductance originates from a large electro-osmotic effect caused by the combination of a very low wall friction and a high negative surface charge[4–6]. However, the origin of this surface charge remains debated. Experimentally, most groups have reported that the ionic conductance displays a strong pH dependence and an unusual power law dependence on the salt concentration c, i.e. $G = c^b$ with b a dimensionless exponent comprised between 0.2 and 0.5. This observation supports a mechanism of surface charge regulation by the electrolyte solution[7,8] that may be related to the specific adsorption of hydroxide ions (OH$^-$) or the protonation of surface groups (e.g., ˇCOOH). Spectral analysis of the ionic current noise would be useful to address these questions, notably to investigate the dynamics of surface charge fluctuations[9] as previously done by Hoogerheide et al.[10] for solid-state nanopores or

[a] *Laboratoire Charles Coulomb (L2C), Univ Montpellier, CNRS, Montpellier, France. E-mail: vincent.jourdain@umontpellier.fr*

[b] *Ukrainian State University of Chemical Technology, 8, Gagarin ave. 49005 Dnipro, Ukraine*

[c] *Laboratoire de Physique Théorique (LPT UMR 5152), Université Toulouse III - Paul Sabatier, CNRS, 31062 Toulouse, France*

[†] Supplementary Information available: [details of any supplementary information available should be included here]. See DOI: 00.0000/00000000.

by Secchi et al.[7] for multi-walled CNTs. However, in the case of individual SWCNTs, such noise analyses were hampered by the difficulty in reliably fabricating SWCNT-based nanofluidic devices and by the low signal-to-noise ratio (S/N) of the reported devices. Although rarely highlighted, the reliable fabrication of SWCNT-based nanofluidic devices remains an experimental *tour de force* often achieved after years of protocol optimization. Consequently, commonly employed materials include standard microfabrication materials such as silicon wafers (SiO_2/Si) as substrates and PMMA (or SU-8) as encapsulating layers. While well-suited for microfabrication purposes, these materials may not always be optimal for physical studies and nanopore sensing applications.

Here, we report on the fabrication and study of individual-SWCNT nanofluidic devices which display a noise reduction of $1-3$ orders of magnitude compared with standard devices. This was achieved by the use of high dielectric constant materials for both the substrate and the CNT-covering layer. In addition, we detail the key points for the successful fabrication of SWCNT-based nanofluidic devices that are reliably leak-free, plug-free, and long-lived, in particular the quality of the substrate-layer interface, the nanotube opening and the removals of photo-resist residues and trapped micro-bubbles. We show that the high signal-to-noise ratio of these devices allows noise spectral analysis of ionic transport through individual SWCNTs, thus evidencing that such narrow and long nanopores keep observing the empirical $1/f$ Hooge's law typical of nanopores [11].

Microdevice fabrication

The developed nanofluidic devices are illustrated in Fig. 1a-e: each device consists of a long individual SWCNT which was grown by lattice-oriented CVD, then transferred to a fused quartz wafer (*i.e.* high-purity amorphous silica) with patterned gold optical marks. Figure 1c shows a SEM image of transferred SWCNTs which is used to select and localize a specific individual SWCNT. A thin layer of SiO_2 (~ 350 nm) is then deposited on the substrate by electron beam evaporation, followed by a thermal annealing at 200°C to improve the layer adhesion. After that, two rectangular reservoirs are etched using reactive ion etching to open the CNT ends and define its length (40 μm) as schematized in Fig. 1b. The protecting photo-resist is dissolved and resist residues are removed using Remover PG and oxygen plasma cleaning. Finally, a thick PDMS layer molded with V-shaped microfluidic channels is sealed on the device by plasma activation and thermal annealing. Each device is made of two symmetric parts: a nanotube device (with an opened SWCNT) and a control device (with no SWCNT): this allows a direct comparison of the responses of SWCNT and control devices with the exact same fabrication history. A photograph of the complete device is given in Fig. 1e, illustrating how the device is connected to fluidic capillaries (two for fluid inlet, two for fluid outlet) and two lab-made silver chloride electrodes (Ag/AgCl), through holes previously punched in the PDMS layer. Fabrication details can be found in the Materials and Methods section.

Achieving high quality interface

The fabrication of a leak-free device requires high-quality interfaces between the different materials. Achieving a tight interface with the top PDMS layer is usually not a problem, since the cleanliness of both surfaces can be well controlled during their fabrication and since well-established protocols, including plasma activation, can be applied to achieve strong PDMS adhesion. The cleanliness of the substrate after CNT deposition is more problematic because CVD growth and CNT transfer are sources of surface contamination (amorphous carbon, photoresist residues) and because CNTs can be damaged by harsh cleaning methods such as plasma cleaning or oxidative annealing. To avoid resist residues, an alternative solution is to use the photo- (or e-beam) resist itself (e.g. SU-8, PMMA) as CNT-covering layer but such polymer layers are prone to leak creation during the plasma opening step [3,4]. This is why we used SiO_2, which has both high chemical resistance and high dielectric strength, as CNT-covering layer.

We found that a major source of reduced adhesion between the SiO_2 layer and the substrate are the resist residuals that remain after liftoff (*i.e.* after creating optical marks). As illustrated by the dark field (DF) image in Fig. 2a, strong detachment of the SiO_2 layer (pink zones) occurs when a standard acetone lift-off is used. At the opposite, SiO_2 adhesion is strongly improved by adding a 15 min exposure to remover PG at 80°C after the acetone lift-off, as shown in Fig. 2b. This evidences that photoresist residuals are the main cause of the reduced adhesion of the CNT-covering layer. Despite the use of remover PG, some detachment remains as evidenced by the purple patches in Fig. 2b. We found that a perfect adhesion could finally be obtained by adding an annealing step at 200°C for 1 hour just after depositing SiO_2, as shown in Fig. 2c. We believe that this annealing step promotes both the formation of strong covalent bonds between the two SiO_2 surfaces, and the diffusion of resist residuals away from the interface region.

SWCNT deposition

We now move to the nanotube deposition step. Until now, most groups have chosen to grow long CNTs directly on the device substrate using gas-flow-aligned CVD (kite growth) [3,12,13]. However, kite-grown CNTs are usually double-walled or triple-walled [13,14], which biases or at least complicates the determination of their inner diameter. In addition, kite growth requires a higher temperature (typically 900-950°C), which restricts the possible materials (substrate, optical marks, electrodes, etc.) and favors pyrolytic carbon contamination. To solve these problems, we have chosen to grow SWCNTs by lattice-oriented CVD [15], which yields long SWCNTs horizontally aligned along a specific direction of the single-crystal growth substrate (here, ST-cut quartz) and to transfer them to the device substrate (fused quartz).

Usually, CNT transfer is achieved by depositing a thin PMMA layer and using a concentrated KOH solution to etch the SiO_2 surface and detach the layer. However, our SEM observations showed that, despite repeated rinsing, this method frequently leaves KOH residuals that corrode the surface of the receiving substrate. Instead, we have found that cellulose acetyl butyrate (CAB), which only requires water for detachment [16] is a much
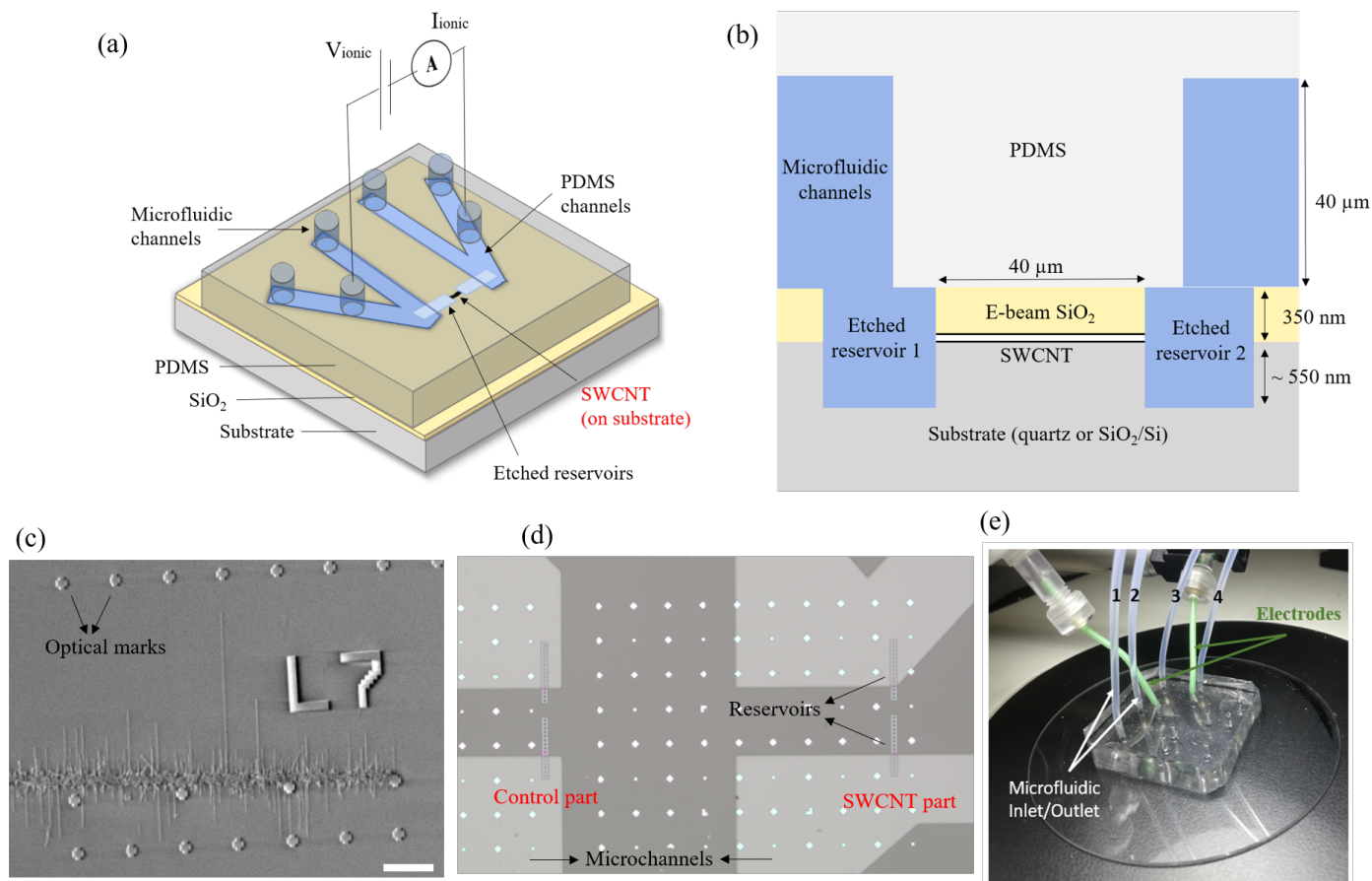
Fig. 1 Nanofluidic device overview. (a) Schematic of the device made of an individual SWCNT on a substrate, covered with a thin SiO_2 layer and connecting two etched reservoirs fed by two microfluidic channels. (b) Side-view image of the nanofluidic device. (c) SEM image of SWCNTs transferred on a substrate with optical marks. (d) Optical image of the complete device (SWCNT and control parts). (e) Photograph of a fabricated device, on quartz substrate, connected to fluidic capillaries and Ag/AgCl electrodes. The scale bar in (c) is 40 μm.
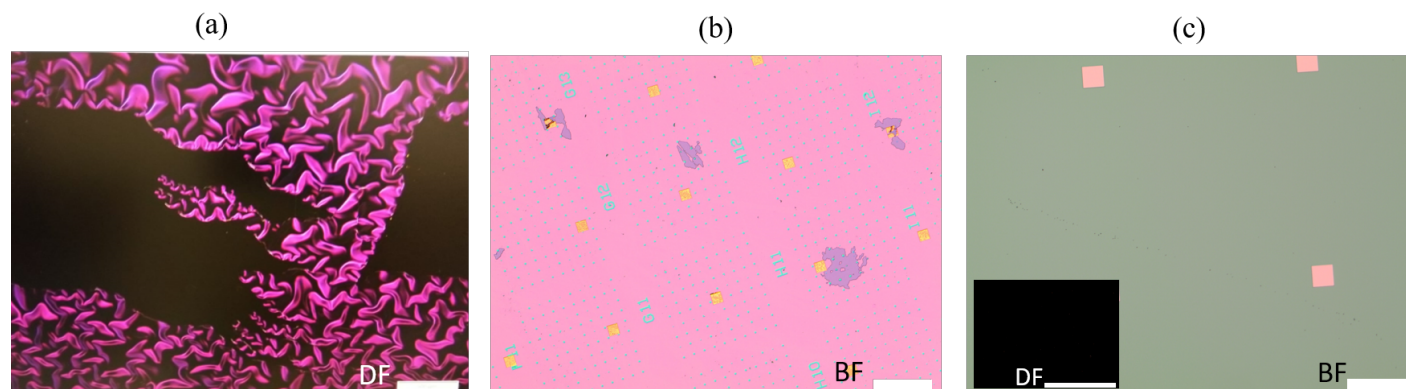

Fig. 2 SiO_2 layer adhesion. Optical microscopy images of the e-beam SiO_2 layer on the fused quartz substrate depending on the protocol of fabrication: (a) after a standard acetone lift-off (dark-field image), (b) with an additional exposure to remover PG (bright-field image), (c) with an additional annealing at 200°C after e-beam deposition (bright-field image); the inset in (c) shows a dark field image displaying null contrast. Scale bars in (a,b,c) are 500 μm, and 100 μm in the inset of (c).

better transfer layer, leaving zero KOH residuals and fewer polymer residuals than PMMA. Note that the annealing step described above also ensures that any CAB residues do not affect the adhesion between the substrate and the CNT-covering layer (here SiO_2).

Microdevice filling

We now move to experimental conditions to ensure that the device is properly filled by the electrolyte solution.

Reservoir filling

The microreservoirs on each side of the nanotube form an important intermediate between the 1 nm scale of the nanotube diameter and the 100 μm scale of the microchannel cross section, the correct filling of which, although generally overlooked, is critical. A common problem is that the reservoirs get plugged by PDMS if a too high mechanical pressure is applied when sealing the top PDMS layer. Fig. 3a-b show optical images of two cases obtained with a high numerical aperture microscope. Fig. 3a corresponds to a device sealed with a high manual pressure, as is commonly done for PDMS microfluidic devices: it can be seen that, under the PDMS wall, there is no difference of color between the reservoirs and the substrate, which means that in both cases, PDMS is in direct contact with the substrate. The contrast does not change during water filling even at pressures up to 1 bar and that such devices display no ionic conductance (< 5 pS).

Instead, we have found that PDMS plugging may be avoided by monitoring the evolution of the reservoir contrast during PDMS alignment and pressing using the optical microscope of a lithography aligner. Using this procedure, one can reliably apply the appropriate pressure needed for well connecting the PDMS layer to the substrate but without plugging the reservoirs. Figure 3b displays plug-free reservoirs whose contrast differs from the rest of the substrate as expected from a thin air layer.

In the case of fused quartz substrates, we found that a good solution to avoid PDMS plugging is to etch deep reservoirs (*i.e.* 900 nm). However, this cannot be done with usual SiO_2/Si substrates because the SiO_2 thickness (which is typically in the range of $100 - 300$ nm) limits the etching depth.

Another common problem is that air bubbles can remain trapped in the reservoirs. Here, we have found that monitoring the filling of the reservoirs in situ using an optical stereomicroscope was the best way to ensure that air was removed from the reservoirs. In Fig. 3c, the pressure applied in the upper microchannel is insufficient and the reservoir remains filled with air. In contrast, the pressure applied in the lower microchannel is sufficient to force air molecules out (by diffusing through the PDMS, which is gas permeable), as evidenced by the gradual change of contrast caused by the change in refractive index between air and water.

Nanotube filling

We have frequently observed that CNT devices initially display negligible ionic conductivity but become markedly conductive following a rinsing of the microchannels with isopropanol (IPA)

(see Figures S1-S2). Since IPA is a well-known hydrocarbon remover, this supports the fact that CNT ends are plugged by polymer residues that redeposited after the dissolution and rinsing steps of reservoir etching. Finally, we have found that the best preparation method, here allowed by the use of an inorganic SiO_2 cover layer, is to perform a plasma resist-cleaning after the etching step, in order to efficiently remove all polymer residues at CNT ends. By adding this plasma cleaning step, all CNT devices initially displayed ionic conductivity without the need for IPA rinsing (see Figure S3). Note that such a thorough plasma treatment would not be possible in the case of a polymer layer (*e.g.* SU-8, PMMA) because it would cause nanofluidic leaks by surface roughening[3,4].

Ionic transport

Figure 4 illustrates the ionic transport measurements for different KCl concentrations in as-prepared devices. As shown in Fig. 4a, the ionic transport on the SWCNT side displays a linear $I - V$ response at all KCl concentrations. This is different from our previous CNT devices with a SU-8 matrix frequently displaying voltage-activated $I - V$ curves, which were also observed for graphene nanopores[17] and we assigned to energy barriers caused by chemical moieties at CNT ends[4]. Here, due to the prolonged plasma opening allowed by the SiO_2 matrix, such activated features are absent and the ionic conductance values are usually higher (by typically one order of magnitude). A typical evolution of the ionic conductance as a function of the KCl concentration is shown in Fig. 4b (red curve): here, the ionic conductance increases from about 40 pS at 10^{-4} M KCl to about 150 pS at 1 M. As typically observed for charged nanopores[4,7], the ionic conductance increases weakly at low salt concentrations then more rapidly at high salt concentrations. This evolution can be related to the transition from surface conductance at low concentration to bulk conductance at high concentration. At the opposite, the conductance on the control side (blue curve) always remains very low (here at around 3 pS) with no or little dependence on the KCl concentration.

To fit the experimental data of Fig. 4b (obtained at $pH = 8.7$), we use the charge regulation theory developed in[8] where the conductance of the electrolyte in the pore was computed assuming a pH-dependent pore surface charge density $\sigma(pH)$: it is the sum of a fixed one σ_f and a pH-dependent one obtained *via* a charge regulation mechanism, $\sigma_R(pH) = \sigma_0/(1 + 10^{pK-pH} e^{|e\psi_s|/kT})$, where σ_0 is the saturation value, pK refers to the equilibrium constant of the charging mechanism and ψ_s is the electrostatic potential at the pore surface. Importantly, it has been shown that fluid slip, which is important for CNTs, contributes to the conductance through an additive term $G = 2\pi Rb\sigma(pH)^2/(\eta L)$ where b is the unknown slip length and η the fluid viscosity. As shown in Fig. 5a a good fit is obtained with the following parameter values: $R = 1.5$ nm, $b = 560$ nm, $\sigma_f = 0.0164$ C/m^2 $\sigma_0 = 0.0197$ C/m^2 and $pK = 8.00$. This pK value is compatible with Fig. S3 where the conductivity is seen to be almost constant for $pH = 4$ and 6, but increases by an order of magnitude at $pH = 10$ (for a KCl concentration of 10^{-2} M). Furthermore, the fitted (negative) mean surface charge density at 10^{-2} M is $\sigma \approx \sigma_f + \sigma_0/2 \approx 0.0262$ C/m^2
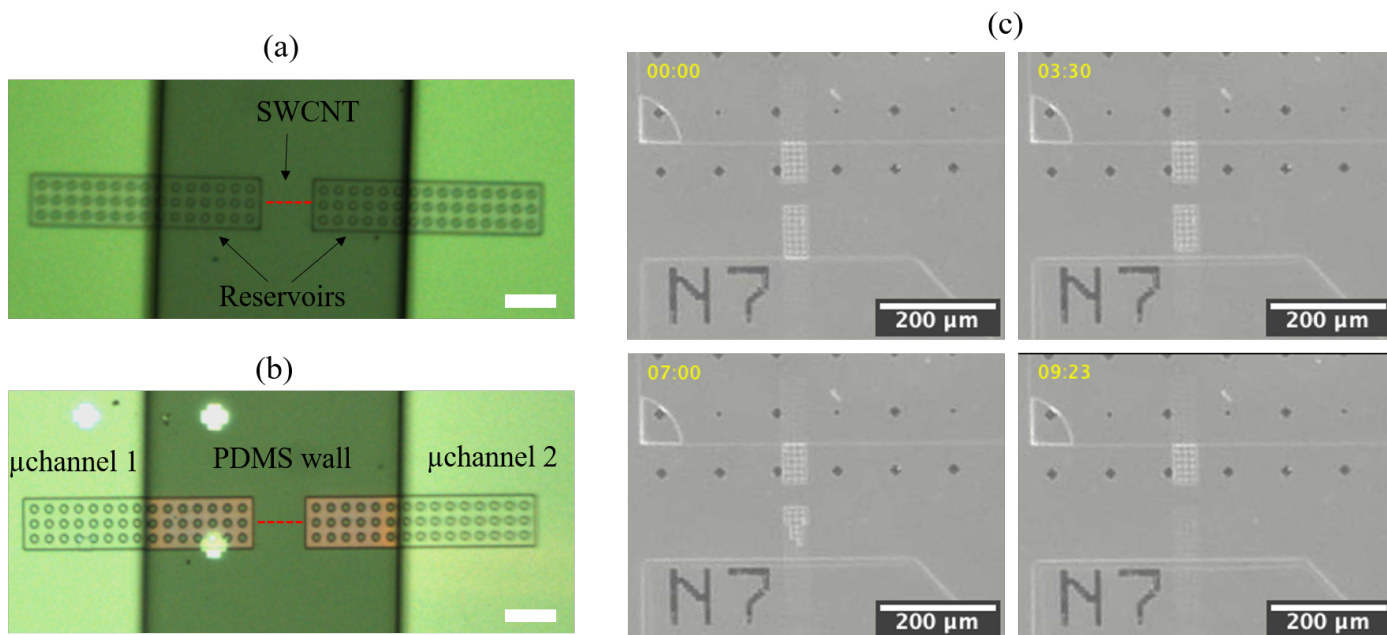
Fig. 3 Plug-free and bubble-free devices. (a,b) Post-fabrication optical microscopy images showing reservoirs (a) plugged and (b) not plugged by PDMS. The scale bars in (a,b) are 40 μm. (c) Images taken with a stereomicroscope during water filling: on these images, a pressure of 200 mbar is applied in the lower channel and no pressure in the upper channel.

in absolute value and therefore compatible with our reversal potential measurements, as we show below.

The reversal potential (RP) is measured by studying the electrolyte conductance through a nanopore as function of an applied voltage difference in the presence of a concentration gradient and extracting the applied potential difference at zero electric current. In line with previous work [5,6], our RP measurements evidence a strong selectivity for cations, *e.g.* with a permeability ratio P_{K^+}/P_{Cl^-} around 35 for this device (see Fig. 5b) in the framework of the semi-phenomenological Goldman–Hodgkin–Katz (GHK) voltage equation used to describe the RP across semi-permeable membranes [18,19]. For a simple salt like KCl the GHK voltage equation for the RP depends only on the salt concentration ratio across the membrane and effective ionic permeabilities that include contributions from the ionic mobilities within the membrane and ionic partition coefficients at the interfaces between the membrane and the external solutions. This approach is not based on a mechanistic model for the membrane, and therefore when applied to a single nanopore, the characteristics of the nanopore do not appear directly but only indirectly in terms of the phenomenological ionic permeabilities. Despite these shortcomings, the GHK approach provides a quick way of characterizing and comparing membrane or nanopore transport properties, in terms of the ratio of effective ionic permeabilities, especially when little is known of the membrane or nanopore characteristics.

By using the physics based Teorell-Meyer-Sievers (TMS) mechanistic approach, however, a direct link can be made between the RP and the physical characteristics of the nanopore, namely the pore radius, R, and surface charge density, σ estimated by fitting our charge regulation model to the conductance measurements [20–23]. The TMS approach, which assumes constant radial ionic concentrations and electric potential (uniform or homogeneous approximation) and neglects electro-osmotic effects, leads to an expression for the RP as the sum of two terms, the Donnan Exclusion Potential and the Henderson Diffusion potential. If one assumes that the ratio of cation and anion mobilities is the same as in the bulk, the TMS prediction for the RP depends only the external salt concentrations and the nanopore volumetric charge density, $X_m = 2\sigma/(eR)$, which itself is a function only of σ and R. Using the values for these last two parameters obtained above by fitting the conductance data, we obtain a volumetric charge density of $X_m = 0.364$ mol/L that leads to a TMS prediction for the RP, presented in Fig. 5b, in very good agreement with the experimental results for concentration ratios below 100. The TMS theory is known to work less well at very high salt concentration ratios where the theory cannot account for the decrease in slope of the *RP vs. external salt concentration ratio* curves (at very high salt concentration ratio the RP can level off, reach a maximum, and then decrease with increasing salt concentration ratio, see e.g., Fig. 8 of Ref. [23]). We see that the GHK and TMS are both useful and complementary approaches, the first being semi-phenomenological and the second physics based. Ionic transport data for other devices are shown in SI (see Figures S1, S2, S3).

A key advantage of using ultrapure silica as matrix (*i.e.* as substrate and cover layer) is to strongly reduce the current noise [24] as was already shown in the case of graphene-based nanopores [25,26]. As shown in Figs. 6a-f, the current noise is decreased at all time scales when fused quartz is used as substrate instead of silicon. To analyze the noise spectrum, we employed the logarithmic power spectral density (LPSD) method [27] which has the advantage of a much better determination of the noise spectrum at high frequency compared with standard power spectrum density (PSD)
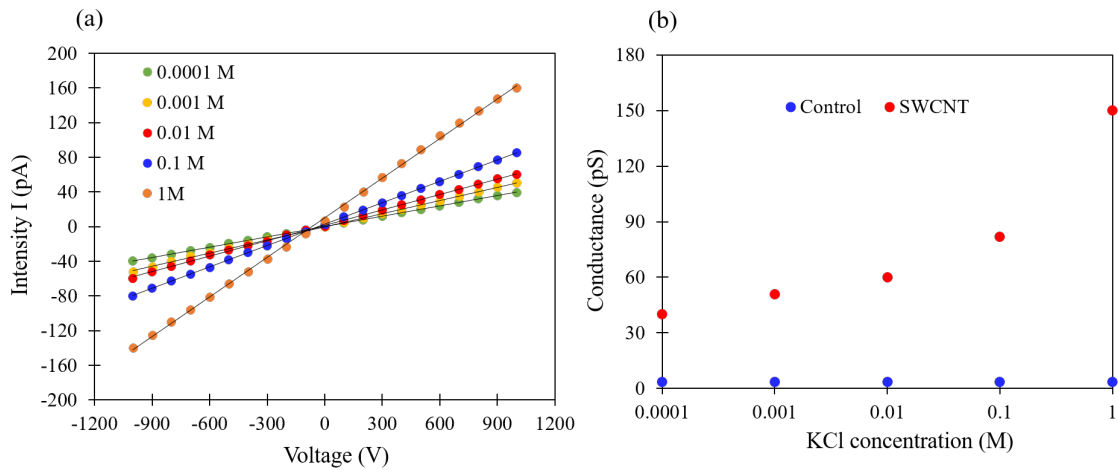
Fig. 4 Ionic transport (Device Q1). (a) Ionic current as a function of applied voltage, for different KCl concentrations (CNT side). (b) Ionic conductance as a function of KCl concentration: CNT (red points) and control (blue points).
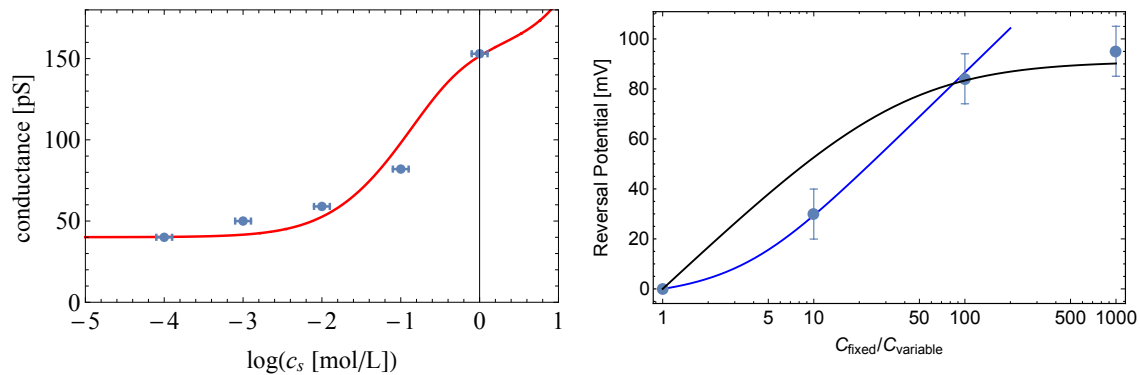

Fig. 5 Theoretical modeling (full lines) of the experimental data obtained on the Q1 device (blue circles). (a) Fit of the KCl conductance data of Fig. 4b (error bars in conductance are within symbol size); Fitting parameters are given in the text. (b) Experimental Reversal Potential (RP) for KCl (blue data points); Teorell-Meyer-Sievers (TMS) prediction (blue curve) for the Reversal Potential (RP) using the pore radius ($R = 1.5$ nm) and surface charge density ($\sigma = 0.0262$ C/m^2) obtained by fitting the charge regulation model to the experimental conduction measurements. Goldman–Hodgkin–Katz (GHK) fit (black curve) with a permeability ratio $P_{K^+}/P_{Cl^-} \approx 35$.

(see comparison in Fig. S5). Figure 6g compares the LPSD spectra of devices that share identical geometry and fabrication protocols, with the only difference being the substrate material (Si/SiO$_2$ or fused quartz): using a fused quartz substrate reduces both the white noise at low frequency (by about an order of magnitude) and the dielectric noise at high-frequency (by $2-3$ orders of magnitude) compared with silicon-based devices.

Figure 6h shows the LPSD of ionic current through a single SWCNT ($V = +1$ V) compared with those in the absence of ionic transport ($V = 0$ V)) and for the control device in the same conditions ($V = +1$ V). LPSDs at other voltages and for another device are shown in Figures S6, S7 and S8. It can be seen that the specific noise signature of ion transport through a single SWCNT is a $1/f$ component at low frequency. For comparison, the same measurements on another device without CNT but with a leak of close conductance (around 1 nS) did not yield $1/f$ contribution (see Fig. S9). More precisely, analysis of all measured noise spectra showed that this low frequency contribution can be fitted by a $1/f^a$ law with a in the range of 1.09 ± 0.16. So, our data well fol-

low the $1/f$ dependence commonly observed for nanopores and described by the empirical Hooge's law:

$$S(f) = \frac{A_H}{f} = \frac{\alpha \bar{I}^2}{f} \tag{1}$$

We also observed a reasonable scaling between A_H and I^2 (see Fig. S10) in agreement with Hooge's law. We also observed high-frequency features (*i.e.* harmonics between 10^2 and 10^4), potentially related to electronic contributions, that were frequently but not systematically observed in combination with the $1/f$ contribution.

Conclusion

In this study, we have detailed protocols for fabricating and analyzing low-noise nanofluidic devices incorporating individual SWCNTs. Using dielectric materials with low-loss properties, we demonstrated the capability to measure the intrinsic noise associated with ionic transport within an individual SWCNT. Our investigations revealed that ionic transport through SWCNTs is pre-
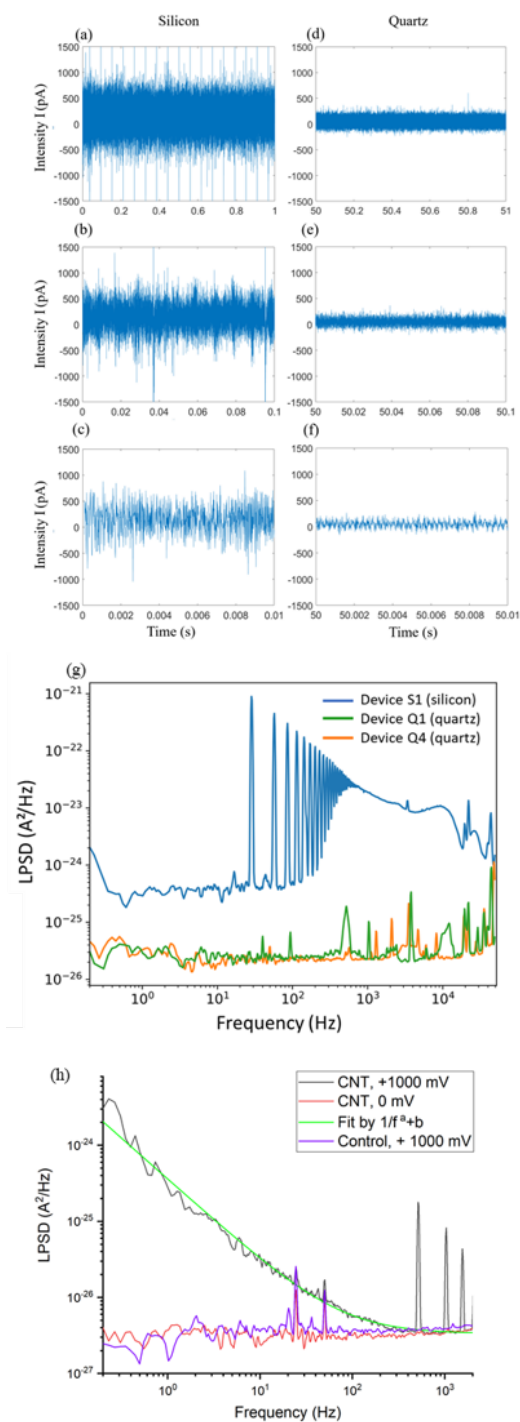
Fig. 6 Noise analysis. (a-f) Current traces for a CNT nanofluidic device on a SiO$_2$/Si substrate (a-c) and on a quartz substrate (d-f) at different time scales. The KCl concentration is 1 M and the sampling rate is 100 kHz in both cases. Devices Q2 (Quartz) and S1 (Silicon). (g) Comparison of the background noise spectra for a device on silicon and two devices on fused quartz substrates ([KCl] = 1 M in all cases)]. (h) LPSD for CNT and control at +1 V (device Q5). This CNT LPSD is best fitted with a power law $1/f^a + b$ with $a = -1.06$ (green curve). The CNT LPSD at 0 V is also shown as reference.

dominantly characterized by a $1/f$ noise component at low frequencies. For SWCNT devices optimized with suitable materials,

we anticipate that this $1/f$ noise will be the ultimate source of noise during individual biomolecule detection *via* nanopore sensing. To effectively mitigate this noise within the typical frequency range of interest ($1 - 100$ Hz) for individual event detection, optimizing the electrolyte concentration and applied voltages to intermediate levels will probably be needed. Specific sensing applications may benefit from the high conductance of SWCNTs at low electrolyte concentrations where white noise is lowest. Further research should aim to refine fabrication techniques, explore other materials, and improve the understanding of $1/f$ noise in SWCNT systems.

Author contributions

LB, SM, ST and CR fabricated the devices. LB, CD, VK, SM, KS and MAK performed the nanofluidic measurements. MM and JP performed the theoretical modeling of the experimental data. FH, AN and VJ coordinated the research.

Conflicts of interest

There are no conflicts to declare.

Data availability

The data supporting this article have been included as part of the Supplementary Information.

Acknowledgments

Materials and Methods

Device fabrication

The used substrates are fused quartz wafers (*i.e.* ultrapure amorphous silica) with thickness of $t = 900$ μm and diameter of $d = 3$ inches. For comparison, devices are also built on doped (N/As) silicon wafers with a 300 nm thermal SiO$_2$ layer (total thickness $t = 381$ μm, diameter $d = 3$ inches). Arrays of optical marks are created on the substrates by photolithography followed by Cr/Au deposition. Long horizontally-aligned SWCNTs are grown on ST-cut single-crystal quartz by catalytic chemical vapor deposition using lattice-oriented growth[4], then transferred to the device substrate using CAB as sacrificial layer[16]. A thin layer of SiO$_2$ (~ 350 nm) is then deposited on the substrate by electron beam evaporation, followed by an annealing at 200°C for 1 hour to improve the layer adhesion. After that, two rectangular reservoirs (40 μm wide, 178 μm long, 900 nm deep) separated by 40 μm are etched at both ends of the SWCNT to open it using reactive ion etching. Before transfer, optical markers (Cr, 10 nm thick) are created by UV lithography on the substrate to localize the nanotubes. The depth of the etched reservoirs is 900 nm in the case of ultrapure silica but only 350 nm in the case of 300 nm SiO$_2$/Si to keep a thick insulating SiO$_2$ layer between the conductive Si substrate and the electrolyte solution. Proper dissolution and removal of the photoresist is critical after etching to avoid nanotube

plugging by photoresist residues: to do so, we first perform dissolution in an acetone bath for 5 min followed by IPA and water rinsing; then the sample is immersed in a Remover PG bath for 5 min followed by IPA and water rinsing; finally, the sample is submitted to an oxygen plasma cleaning during 5 min.

Ionic transport measurements

Ionic current measurements were made using an Axopatch 200B current amplifier. Flows were controlled using a four-channel pressure-based microfluidic flow controller (Fluigent MCF-4C). All measurements were performed inside a Faraday cage installed on a damped optical table. Before ionic measurements, the microchannels were washed with MQ water for 15 minutes. In the cases where the initial ionic conductance was very low (< 10 pS), isopropyl alcohol (IPA) was additionnally flown in the microchannels for 5 min to dissolve photoresist residuals or airborne hydrocarbons plugging CNT ends.

A stereomicroscope (Leica S9i) was used to monitor the filling and ensure that the reservoirs were completely filled without trapped bubbles. During ion current measurements, the microscope was electrically disconnected from the outside of the Faraday cage to keep high electromagnetic screening. The ionic current of the device was recorded using potassium (chloride (KCl) solutions with different concentrations (10^{-4}, 10^{-3}, 10^{-2}, 10^{-1} and 1 M) using a voltage range of ± 1 V. The ionic current was recorded for at least 10 min to ensure that the new solution had replaced the previous one as assessed by in situ monitoring of the ionic current. To allow for rigorous comparison, the control and the CNT parts were subjected to exactly the same preparation procedure, and the same measurements were performed on the CNT and control parts.

Notes and references

1 S. Zhang, L. Kang, X. Wang, L. Tong, L. Yang, Z. Wang, K. Qi, S. Deng, Q. Li, X. Bai, F. Ding and J. Zhang, *Nature*, 2017, **543**, 234–238.

2 M. Manghi, J. Palmeri, F. Henn, A. Noury, F. Picaud, G. Herlem and V. Jourdain, *Journal of Physical Chemistry C*, 2021, **125**, 22943.

3 H. T. Liu, J. He, J. Y. Tang, H. Liu, P. Pang, D. Cao, P. Krstic, S. Joseph, S. Lindsay and C. Nuckolls, *Science (Washington, D. C., 1883-)*, 2010, **327**, 64–67.

4 K. Yazda, S. Tahir, T. Michel, B. Loubet, M. Manghi, J. Bentin, F. Picaud, J. Palmeri, F. Henn and V. Jourdain, *Nanoscale*, 2017, **9**, 11976–11986.

5 P. Pang, J. He, J. H. Park, P. S. Krstic and S. Lindsay, *ACS Nano*, 2011, **5**, 7277–7283.

6 H. Amiri, K. L. Shepard, C. Nuckolls and R. Hernández Sánchez, *Nano Letters*, 2017, **17**, 1204–1211.

7 E. Secchi, A. Nigues, L. Jubin, A. Siria and L. Bocquet, *Physical Review Letters*, 2016, **116**, 154501.

8 M. Manghi, J. Palmeri, K. Yazda, F. Henn and V. Jourdain, *Physical Review E*, 2018, **98**, 012605.

9 S. Gravelle, R. R. Netz and L. Bocquet, *Nano Letters*, 2019, **19**, 7265–7272.

10 D. P. Hoogerheide, S. Garaj and J. A. Golovchenko, *Physical Review Letters*, 2009, **102**, 256804.

11 A. Fragasso, S. Schmid and C. Dekker, *ACS Nano*, 2020, **14**, 1338–1349.

12 C. Y. Lee, W. Choi, J. H. Han and M. S. Strano, *Science (Washington, D. C., 1883-)*, 2010, **329**, 1320–1324.

13 G. Cui, Z. Xu, H. Li, S. Zhang, L. Xu, A. Siria and M. Ma, *Nature Communications*, 2023, **14**, 2295.

14 Z. Zhu, N. Wei, W. Cheng, B. Shen, S. Sun, J. Gao, Q. Wen, R. Zhang, J. Xu, Y. Wang and F. Wei, *Nature Communications*, 2019, **10**, 4467.

15 J. Xiao, S. Dunham, P. Liu, Y. Zhang, C. Kocabas, L. Moh, Y. Huang, K. C. Hwang, C. Lu, W. Huang and J. A. Rogers, *Nano letters*, 2009, **9**, 4311–4319.

16 G. F. Schneider, V. E. Calado, H. Zandbergen, L. M. K. Vandersypen and C. Dekker, *Nano Letters*, 2010, **10**, 1912–1916.

17 T. Jain, B. C. Rasera, R. J. S. Guerrero, M. S. H. Boutilier, S. C. O'Hern, J.-C. Idrobo and R. Karnik, *Nat Nano*, 2015, **10**, 1053–1057.

18 D. E. Goldman, *The Journal of General Physiology*, 1943, **27**, 37–60.

19 A. L. Hodgkin and B. Katz, *The Journal of Physiology*, 1949, **108**, 37–77.

20 T. Teorell, *Proceedings of the Society for Experimental Biology and Medicine*, 1935, **33**, 282–285.

21 K. H. Meyer and J. F. Sievers, *Helvetica Chimica Acta*, 1936, **19**, 649–664.

22 G. B. Westermann-Clark and C. C. Christoforou, *Journal of Electroanalytical Chemistry and Interfacial Electrochemistry*, 1986, **198**, 213–231.

23 A. H. Galama, J. W. Post, H. V. M. Hamelers, V. V. Nikonenko and P. M. Biesheuvel, *Journal of Membrane Science and Research*, 2016, **2**, 128–140.

24 S. Liang, F. Xiang, Z. Tang, R. Nouri, X. He, M. Dong and W. Guan, *Nanotechnology and Precision Engineering*, 2020, **3**, 9–17.

25 A. Kumar, K.-B. Park, H.-M. Kim and K.-B. Kim, *Nanotechnology*, 2013, **24**, 495503.

26 L. J. de Vreede, C. Ying, J. Houghtaling, J. Figueiredo Da Silva, A. R. Hall, A. Lovera and M. Mayer, *Nanotechnology*, 2019, **30**, 265301.

27 M. Tröbs and G. Heinzel, *Measurement*, 2006, **39**, 120–129.